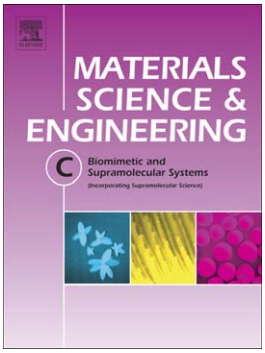

Nanoindentation Analysis of α Tricalcium Phosphate-Poly(lactide-co-glycolide) Nanocomposite Degradation

C.E. Barrett, R.E. Cameron

PII: S0928-4931(14)00309-9
DOI: doi: 10.1016/j.msec.2014.05.033
Reference: MSC 4657

To appear in: *Materials Science & Engineering C*

Received date: 22 March 2014
Accepted date: 7 May 2014

Please cite this article as: C.E. Barrett, R.E. Cameron, Nanoindentation Analysis of α Tricalcium Phosphate-Poly(lactide-co-glycolide) Nanocomposite Degradation, *Materials Science & Engineering C* (2014), doi: 10.1016/j.msec.2014.05.033

Nanoindentation Analysis of αTricalcium Phosphate-Poly(lactide-co-glycolide) Nanocomposite Degradation

C.E. Barrett*, R.E. Cameron

Cambridge Centre for Medical Materials, Department of Materials Science and Metallurgy, University of Cambridge, 27 Charles Babbage Road, Cambridge, UK, CB3 0FS

Abstract

The internal mechanical property characteristics as functions of position and degradation time of PLGA(50:50)-αTCP nanocomposites of varying ceramic-polymer ratios degraded in an aqueous medium have been assessed using depth-sensing nanoindentation.

The addition of nanoparticulate αTCP increases the elastic modulus of undegraded specimens from 3.72 $\pm$ 0.12 GPa for pure PLGA(50:50) samples to 7.23$\pm$0.16 GPa recorded for undegraded 40 wt% TCP nanocomposites. Additionally αTCP incorporation decreases the viscoelastic loss tangent from 0.189 ± 0.040 measured for pure undegraded PLGA(50:50) to an average of 0.091 ± 0.006 for undegraded ceramic-polymer composites. No variation in viscosity for the composites with ceramic loading was evidenced.

The stiffening effect of αTCP addition closely conforms to the lower Hashin-Shtrickman bounds demonstrating that an evenly dispersed nano-filler is the least amenable ceramic configuration enhance the mechanical properties of PLGA-αTCP nanocomposites.

The mechanical property evolution for all composite types in an aqueous degradation medium is dominated by material hydration which effects reduced material stiffness and increased specimen viscosity generating a core-periphery mechanical property distribution in terms of elastic modulus and viscoelastic phase angle. The mechanical property core-periphery structure correlates strongly with the core-periphery density structure characterized using X-ray microtomography. Hydrated regions exhibit significant reductions in elastic modulus and viscosity increases which are typical of elastomers.

Keywords: Poly(lactic-co-glycolic) acid, Calcium phosphate, Nanocomposite, Nanoindentation, Mechanical properties

*Corresponding author, e_mail: cebaz577@gmail.com, tel: (0044) 07963011934

1 Introduction

Systematic characterization of mechanical properties of degradable biomaterials is a salient problem in modern biomedical materials research [1]. The dearth of quantitative polymer degradation and erosion rates in addition to the absence of information regarding mechanical property evolution with specimen type and degradation time is a significant hindrance to material modelling, prediction and optimization of biodegradable device performance [2].

The principal obstacle to material degradation characterization is the small length scales associated with degradation phenomena which limits the effectiveness of conventional methods to evaluate mechanic properties. This difficulty is pertinent to the characterization of the degradation kinetics of nanoparticulate α-tricalcium phosphate - poly(lactic-co-glycolic) acid composites (50:50 monomer ratio) which are candidate materials for use in orthopaedic devices. Systematic position-dependent mechanical property characterization of the material as function of degradation time and ceramic loading is lacking in the literature. The rationale behind nanocomposite development for this material and other similar specimens was reviewed by Barrett *et al.* [3] and preliminary assessments of composite degradation behaviour and biological assays may be found in references [4]-[5]-[6].

Nanoindentation was chosen as the testing method for mechanical property assessment due to the small specimen size and length scales associated with degradation induced mechanical property changes which are not amenable to mechanical property measurements using standard techniques used to evaluate bulk materials. Moreover, measurement of water imbibition effects requires high spatial resolution which is achievable using a nanoindenter system.

2 Background

Introductions to the nanoindentation technique may be found in the bibliography [7][8]. Briefly, the nanoindentation technique relies on measurement of the material stiffness which is defined by Sneddon [9] as

$$S = \frac{\mathrm{d}P}{\mathrm{d}h} \tag{1}$$

where $\mathrm{d}P$ and $\mathrm{d}h$ denote the change in load and displacement respectively.

For sufficiently small harmonic displacement oscillation amplitudes, discounting adhesion between the nanoindenter and the test material [10], quasi-static and harmonic displacements may be decoupled. Neglecting indenter deformation and using the linear viscoelastic correspondence principle, $E = E^{'} + iE^{''}$, nanoindentation measured storage and loss moduli are calculated using

$$\frac{E^{'}}{1-\nu^2} = S\frac{1}{2\beta}\frac{\sqrt{\pi}}{\sqrt{A}}\cos\phi \tag{2}$$

and

$$\frac{E^{''}}{1-\nu^2} = S\frac{1}{2\beta}\frac{\sqrt{\pi}}{\sqrt{A}}\sin\phi \tag{3}$$

respectively [11, 12] where S represents the harmonic contact stiffness, A denotes the indenter contact area with the sample. β is an indenter geometrical term which is equal to $\beta = 1$ for flat circular punch, spherical and conical indenters and $\beta = 1.034$ for a Berkovich indenter [7]. The phase delay between the harmonic load and the material displacement is denoted by the loss angle, ϕ.

The Poisson's ratio, ν, is unknown for the materials investigated in this work, a situation which is commonly encountered in indentation measurements. The Poisson's ratio is also dependent on the nanocomposite type, degradation state and for viscoelastic materials varies according to the nanoindentation strain rate, frequency of modulation, temperature and time. A review of such issues was performed by Tschoegl *et al.* [13]. Generally, accurate knowledge of the Poisson's ratio is a desirable but not a necessary criterion for accurate nanoindentation measurements. A 25% uncertainty in the value of ν yields errors in the elastic modulus of approximately 15% for $\nu = 0.5$ and around 8% for $\nu = 0.4$.

Throughout this work a value of $\nu = 0.4$ was used for all nanoindentation tests.

2.1 Viscoelastic effects

The previous discussion of measured material stiffness has neglected the effects of specimen viscosity which is likely to represent a significant deformation mode for the nanocomposites especially as degradation proceeds. Load-displacement analysis in both quasi-static and dynamic modulation mode is affected by creep displacement which produces continued forward indenter displacement during the unloading segment. *In extremis*, creep may yield a negative unloading stiffness known as a "nose"; even moderate viscoelastic deformation can cause higher unloading gradients yielding greater elastic moduli if the stiffness is evaluated at the unloading point [14]. Creep also contributes to incorrect indentation area determination [15].

Ngan and Feng [16] evaluated the Berkovich nanoindentation behaviour of polypropylene using material relationships predicated on the linear viscoelastic correspondence principle. Assuming non-decreasing indenter penetration, simulations demonstrated that nosing occurs when

$$\frac{P_{max}}{|\dot{\nu}_{unload}|} > \frac{4\sigma\left(1-\nu^2\right)}{3\dot{\varepsilon}E} \tag{4}$$

where P_{max} is the peak load, $\dot{\nu}_{unload}$ the unloading velocity, ν the Poisson's ratio, E the elastic modulus and σ and $\dot{\varepsilon}$ the material stress and strain rate respectively. The inequality in equation 4 is satisfied for slow unloading, insufficient creep dwell times and excessive peak load (P_{max}). This result was corroborated by Cheng *et al.* [17] which demonstrated that the empirical spherical and conical indentation behaviour of viscoelastic materials achieves optimal agreement with linear viscoelastic indenter simulations when a creep-hold regime prior to fast unloading is used.

Following Ngan and coworkers [14, 15, 18], the measured unloading stiffness for a viscoelastic material (S_{app}) is related to innate material stiffness, S, and the viscoelastic contribution, S_{creep} according to

$$\frac{1}{S_{app}} = \frac{1}{S} - \frac{1}{S_{creep}} = \frac{1}{S} - \frac{\dot{h}_{creep}}{\left|\dot{P}_{unload}\right|} \tag{5}$$

where $\dot{h}_{creep}$ and $\dot{P}_{unload}$ represent the creep velocity and the unloading rate respectively.

In this investigation, the harmonic load amplitudes are typically $1 - 10\mu$N operating at 45 Hz equating to an approximate unloading time of 0.005 seconds hence $|\dot{P}_{unload}| \approx 1.5\,\mathrm{mN{\cdot}s^{-1}}$. The most compliant viscoelastic materials tested exhibit an approximate creep velocity at the start of unloading of around $15\mathrm{nm}\cdot\mathrm{s}^{-1}$. The creep contribution to displacement is therefore approximately $S_{creep} \approx 6.7 \times 10^4\,\mathrm{Nm}^{-1}$ compared with typical apparent harmonic stiffness values of $S_{app} \approx 1.5 \times 10^3\,\mathrm{Nm}^{-1}$ therefore

$$\frac{1}{S_{app}} \gg \frac{1}{S_{creep}} \tag{6}$$

demonstrating that under the dynamic modulation testing conditions used in this investigation (see section 3.2) creep effects can be assumed to be negligible.

An additional concern that heat dissipation during dynamic modulation may increase material compliance was shown to be negligible by Vanlandingham [19] for glassy polymers and elastomers which have the range of properties exhibited by PMNCs for oscillation amplitudes larger than those used in this investigation.

3 Experiment

3.1 Specimen fabrication

Phase pure α TCP was synthesized at room temperature using an aqueous precipitation reaction described by

$$2H_3PO_{4\{aq\}} + 3Ca\,(OH)_{2\{aq\}} \rightarrow Ca_3\,(PO_4)_{2\{aq\}} + 6H_2O. \quad (7)$$

0.187 M calcium hydroxide (Sigma Aldrich, UK) and 0.121 M orthophosphoric acid, H_3PO_4 (analytical reagent grade, BDH Laboratory Supplies, UK) were stirred separately for one hour and then mixed and stirred together for another hour. The solution was left to age for 24 hours then the precipitate was filtered and dried. αTCP was produced by sintering the filtered powder at 1400°C for four hours followed by rapid cooling to room temperature.

Tricalcium phosphate phase composition was assessed using X-ray powder diffraction (Philips X-Pert PW3020 vertical diffractometer) over the diffraction angle range $10° - 50°$ using a step size of 0.02° and dwell time of 30 seconds. The diffractometer employed Cu K_α X-rays operating at source voltage and current settings of 40 kV and 40 mA. Phase identification was performed by fitting crystallographic diffraction patterns for αTCP, βTCP and hydroxyapatite in addition to known contaminants such as CaO to the empirical powder diffraction pattern using the software Highscore Plus which used the reference intensity ratio method. This demonstrated that the phase purity of the TCP α polymorph was >95% which meets the required criterion for phase purity.

Ceramic crystal size evaluation was performed using X-ray peak broadening analysis according to the full-width half maximum version of the Scherrer formula which relates the crystal diffraction peak full-width half maximum, γ, from a crystal of width d according to

$$d = \frac{K\lambda}{\gamma cos(2\theta)} \quad (8)$$

where λ the wavelength measured in nanometres and 2θ the Bragg angle (in radians). An intermediate value of the Scherrer constant of $K = 0.9$ was used although significant deviations may occur from this value for some crystal shapes [20].

The instrument mediated peak broadening as a function of scattering angle was determined by linear interpolation between instrument broadening measured for large-crystal silicon added to the powder sample which exhibits diffraction peaks at 28.3° and 47.2° neglecting possible non-linearity of diffraction profiles with Bragg angle. This analysis demonstrated that the crystal axes corresponding to the most intense diffraction peaks were in the $20 - 50$ nm range.

PLGA(50:50)-αTCP nanocomposites containing weight fractions of 10, 20 30 and 40 wt% ceramic were formed using a solvent evaporation method with prior ball and attritor milling for 4 hours in acetone to reduce the TCP particle size and generate an even ceramic distribution. The material was formed into nominally 900 μm thick sheets by compression molding. Disks of diameter 8 mm were cut from the sheet using a circular punch.

Although Scherrer analysis demonstrates a mean nanometric αTCP crystal size, particle agglomeration occurs in the composite which requires assessment. This was performed by Wilberforce *et al.* [21] using a cold cathode field emission electron SEM (S-5500, Hitachi, Japan). Samples differed from those studied in this investigation in that injection molding rather than compression molding was used in specimen manufacture after the attritor milling procedure. Modal particle sizes for 10, 20 and 30 wt% composites were $\leq$ 150 nm and $\leq$ 225 nm for 40 wt% composite. Nonetheless, the particle dispersion in 40 wt% composites is significant with an appreciable number of ceramic particles possessing mean crystal dimensions greater than 500 nm. Nevertheless, the ceramic particle size distribution indicates that a nanocomposite and not a microcomposite is formed using composite fabrication process described.

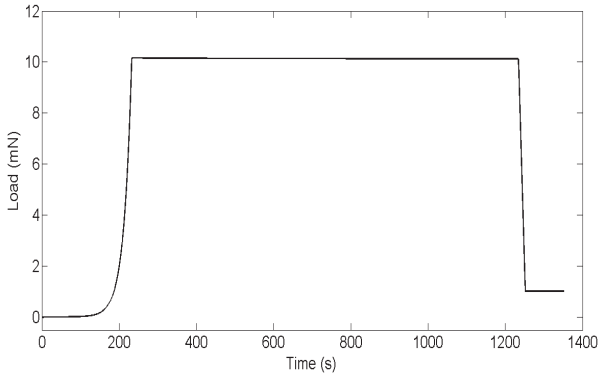

Figure 1: Nanoindentation quasi-static loading routine showing constant $0.05\,s^{-1}$ strain-rate loading followed by a load-hold segment prior to unloading. During the loading segment a small oscillation is applied to the indenter ($\Delta h \approx 2$ nm) which is too small to be resolved on the figure.

Specimens were degraded in 40 ml distilled, deionized water at 37.4°C (the approximate undegraded sample to water volume ratio was 1:900). At designated time points samples were removed from the study and embedded in epoxy resin (Struers Epofix) and left to cure for 12 hours.

Nanocomposites and PLGA(50:50) specimen transects were prepared for indentation testing by sectioning embedded samples using a Struers Accutom employing a

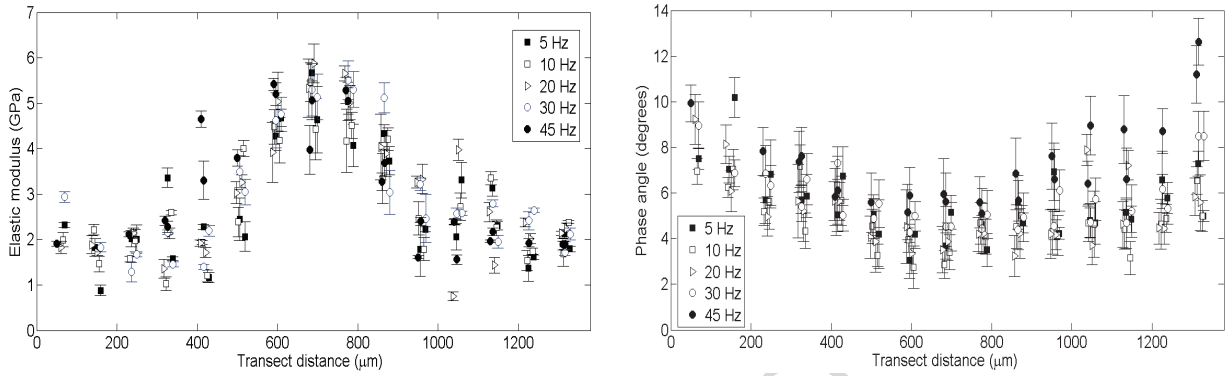

(a) (b)

Figure 2: Dynamic modulation measured (a) elastic modulus and (b) phase angle for 40 wt% nanocomposite degraded for 21 days (transect width 1369 μm) tested using dynamic modulation frequencies of 5, 10, 20 30 and 45 Hz.

12240 diamond cutting wheel operating at 3000 rpm. Non-planar surface topographic errors on the calculated indenter contact area, A, were mitigated by surface polishing of samples prior to indentation according to the ASTM E3-80 recommendations [22]: nanoindentation performed over depths greater than 1000 nm require a 1 μm diamond polish. Samples were mechanically polished on a series of polishing mats of progressively diminishing grit size (400, 800, 1200 and 2500) washing between stages to prevent cross-contamination. Finally samples were polished using a 1 μm diamond paste producing a good mirror finish.

After sectioning the PLGA and nanocomposites dried in air rapidly prior to the execution of nanoindentation testing therefore all results represent dehydrated materials.

3.2 Nanoindentation testing methodology

All dynamic modulation nanoindentation tests in this investigation employed a NanoIndenter XP (MTS Nano Instruments, Oak Ridge, TN, USA) utilizing the continuous stiffness measurement (CSM) technique which is theoretically capable of force and displacement resolution of 50 nN and 0.01 nm respectively. Samples were positioned on a lateral motion stage with nominal lateral 2 μm resolution mounted on a vibration reduction table. Indentation experiments were conducted using a spherical sapphire indenter of nominal radius 10.37 μm. A spherical indenter was used to avoid the difficulties in mounting a flat-punch indenter normal to the test surface and the high strains generated by the Berkovich indenter which complicates initial contact point determination for sharp indentation of compliant materials. Moreover, for sufficiently large radius spherical indenters, the Tabor contact strain [23] may be sufficiently small to permit the application of the small-stain linear viscoelastic approximation. Disadvantages of spherical indenter utilization includes changing contact areas with harmonic oscillatory motion.

All indentation experiments were performed according to the quasi-static load-time history detailed in figure 1 with the indenter operating in load control mode and displacement the dependent variable. All indentation tests utilized a quasi-static loading strain-rate and loading displacement target of $0.05\,\mathrm{s}^{-1}$ and 2000 nm respectively followed by a 1000 s load-hold regime used to assess creep displacement which is discussed in a subsequent article.

During the unloading phase at 10% of the maximum load, a second load-hold regime was applied for approximately 100 seconds to assess indenter drift resulting from viscoelastic creep or thermal fluctuations in the sample-indenter assembly. The lower load is used to minimize creep or time-dependent plasticity displacement contributions. Nonetheless, it is not known whether nanocomposite viscoelasticity can be neglected at low load hence thermal correction was not performed.

Dynamic modulation was performed at a constant frequency of 45 Hz (corresponding to an approximate unloading time of 0.01 s) using a fixed target oscillation amplitude of $\Delta h = 2\,\mathrm{nm}$ (actual recorded values during experimentation were approximately 80% of those prescribed). The small amplitude of 2 nm is used to limit potential non-linear viscoelastic material behaviour and to minimize the "tapping error" characterized by loss of indenter contact for shallow indents [24].

Surface detection was performed automatically using the gating condition of an 8% increase in stiffness compared with the reference value of the indenter oscillating freely during surface approach. In general, the user-corrected contact point is a better estimate of the initial contact displacement than automatically generated values. Surface zero point correction was performed manually after each test series for all indents using either continuous stiffness or viscoelastic phase angle measure-

Specimen	E (GPa)	H (GPa)	$\phi_{exp}(^\circ)$	VR (GPa)	VR (ϕ)	HS (GPa)
PLGA	3.72±0.19	0.085±0.010	10.7±2.2	-	-	-
10 wt%	5.32 ±0.10	0.238±0.014	5.56 ±0.22	5.2	10.5°	5.4
20 wt%	5.99 ±0.18	0.237±0.005	5.26 ±0.22	5.5	10.5°	5.9
30 wt%	6.58 ±0.12	0.200±0.010	5.27 ±0.23	5.8	10.4°	6.6
40 wt%	7.23±0.16	0.259±0.003	4.74 ±0.04	6.3	10.4°	7.5
50 wt%	-		-	6.9	-	8.7

Table 1: Elastic moduli (E), indentation hardness (H) and viscoelastic phase angles (ϕ) measured for all undegraded composite types investigated in addition to calculated Voigt-Reuss (VR) and Hashin-Shtrikman (HS) composite elastic moduli and viscoelastic phase angle lower bounds.

ments. Nonetheless, dynamic modulation phase and harmonic contact stiffness are continuously varying properties which complicates precise surface contact point determination particularly for degraded, highly compliant materials.

3.2.1 Tip calibration

Indenter tip area determination as a function of indentation depth was performed prior to each nanoindentation experiment using an indirect measurement technique. The contact area (and hence elastic modulus) was least-squares fitted as a function of contact depth to an area-indentation depth relationship parametrized as a polynomial containing ten terms of the form

$$A\left(h_c\right) = C_0 h_c^2 + C_1 h_c + C_2 h_c^{\frac{1}{2}} + C_3 h_c^{\frac{1}{4}} + ... \qquad (9)$$

where C_i denote coefficients to be optimized as functions of contact depth, h_c .

A minimum of 20 calibration indents were made on single crystal silicon reference (E = 72±2 GPa, $H = 9\,\mathrm{GPa}$, $\nu = 0.18$) using the instrument operation mode described in section 3.2 and data outputted to the software package "ANALYST" (MTS Nano Instruments, Oak Ridge, TN, USA) which employs an area calibration fitting routine based on the Oliver-Pharr [11] procedure.

The constants C_i were optimized in equation 9 to best match the acquired moduli versus displacement values by χ^2 minimization weighted towards large displacements ($h > 1000\,\mathrm{nm}$). After each testing series, several indents were made on the reference to verify that the indenter geometry remained invariant during testing.

3.2.2 Indent depth effects

Most indents executed on PMNCS exhibited significant modulus and phase angle variations with indentation depth over the first several hundred nanometers into the specimen surface stabilizing at an indentation depth of approximately 600 nm.

Factors which retarded stabilization may be tip geometrical errors (calibration data are given higher weighting in the 1000 - 2000 nm depth range), which are most prominent for shallow indents. Vanlandingham [25] demonstrated that indirect area measurements are generally depressed compared with the true areas at shallow indentation depths which may exacerbate modulus variations.

An additional factor in dynamic modulus and hardness variations for small displacements is imprecise surface detection which may disrupt load or strain rate control mechanisms. This is most important during the transition from indenter surface approach mode to constant strain rate loading which only becomes effective when the indenter is displaced approximately 100 nm into a sample [25].

An additional source of the variation in material properties with indentation depth is the indentation size effect which is well documented for metals [26]. Isolation of the indentation depth effect by Nix and Gao [27] from indenter irregularities, surface roughness and imperfect surface detection generated an indentation hardness-depth relationship demonstrating that the indentation size effect is significant in metals for indentation depths less than 100nm [28]. Less information exists for polymers, nonetheless, similar behaviour is evident [29]. Generally, the indentation size effects for aromatic polymers occurs for $h \leq 500$ nm which is significantly larger than in aliphatic polymers. The indentation size effect for PLGA therefore is likely to be negligible for depths > 300nm and therefore is mitigated by the higher weighting given to data acquired for $h > 1000\,\mathrm{nm}$.

4 Degradation experiment

4.1 Preliminaries

Viscoelastic material property frequency dependence was evaluated on a representative 40 wt% composite degraded for 21 days according to section 3.1 and tested according to section 3.2. Approximately 20 indents were executed across specimen transects using a spherical 10.37 μm radius sapphire indenter at a constant strain rate of $0.05\,\mathrm{s}^{-1}$.

Elastic moduli and viscoelastic phase angles measured for harmonic indentation frequencies of 5, 10, 20, 30 and

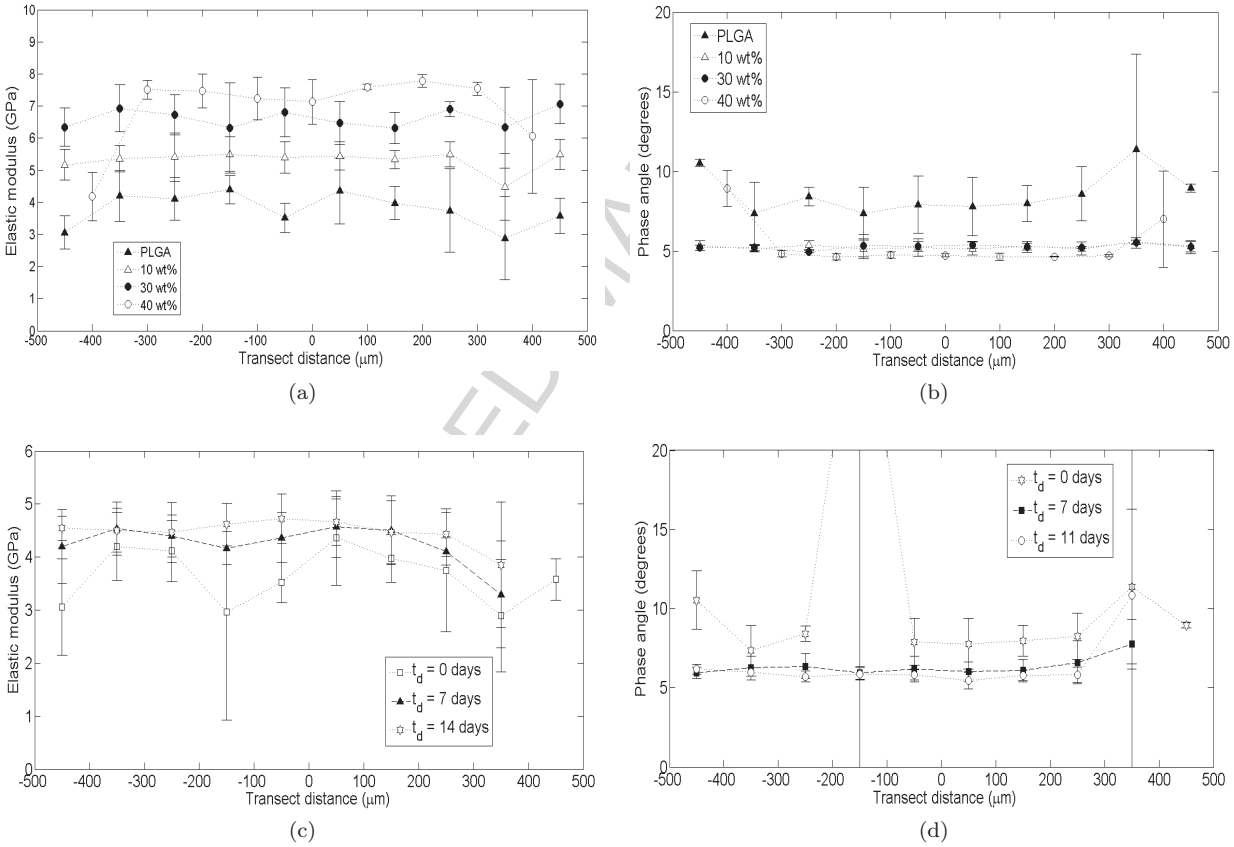

Figure 3: Mean values of (a) elastic modulus and (b) viscoelastic phase angle across transects of undegraded PLGA(50:50) and nanocomposites tested using nanoindentation. The variation in pure PLGA elastic and viscoelastic properties with degradation time are presented in (c) and (d) respectively.

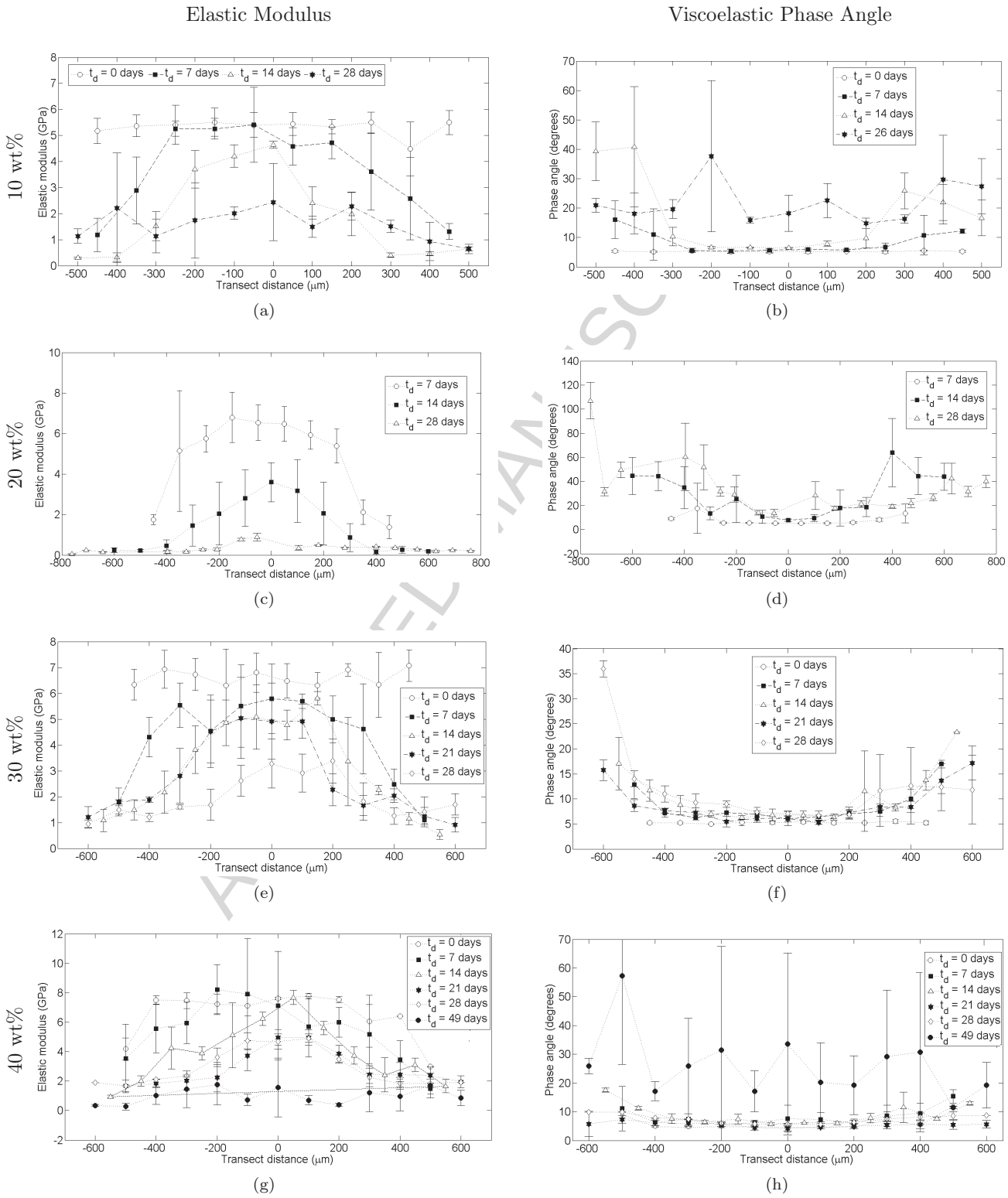

Figure 4: Dynamic modulation nanoindentation measured mean values of elastic modulus and viscoelastic phase angle across transects of 10, 20, 30 and 40 wt% nanocomposites at varying degradation times. The reduction in material elastic moduli with degradation time is clearly evident for each composite type. Viscoelastic phase angle data also show a peripheral-core structure although the transition between the two regions is less pronounced compared with modulus data.

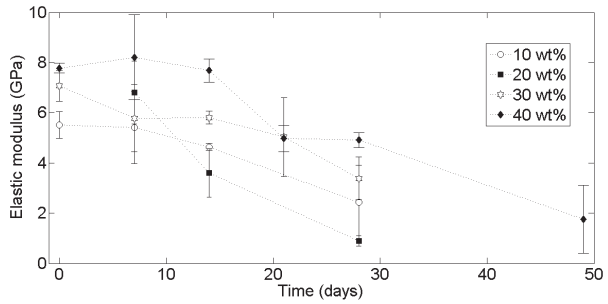

Figure 5: Peak elastic moduli versus degradation time of nanocomposite core regions measured using dynamic modulation nanoindentation.

45 Hz. are shown in figure 2. No significant differences in elastic modulus (figure 2a) can be observed with frequency. A trend does appear in the figure where the viscoelastic loss angle acquired at 45 Hz appears consistently greater than equivalent data for the experiment performed at 5 Hz across the transect. Nevertheless, differences are typically maintained to within the uncertainty associated with each test at the equivalent transect position. Based on this survey there appears to be an insignificant difference between material properties acquired at various dynamic oscillation frequencies. hence a dynamic modulation frequency of 45 Hz was be employed throughout CSM testing.

4.2 Results

The large number of tests executed across specimen transects is not amenable to comparisons between specimen types and degradation stages. Instead tests are compiled into transects bins of width 100 μm for which bin average and standard deviation values are calculated.

Transect distances were measured relative to two reference positions on the edge of each transect. Some transect position error arises from specimen warping which becomes increasingly pronounced with material degradation time.

Average elastic moduli and viscoelastic phase angles of undegraded PLGA and nanocomposites are presented in figures 3a and 3b. Averaged transect values of elastic modulus, phase angle and hardness are presented in table 1 in addition to bi-phasic material model mechanical property limits which are discussed in section 5.

The average value of the viscoelastic phase angle for nanocomposites in the undegraded state is $5.18 \pm 0.14°$ compared with $8.63 \pm 1.28°$ for PLGA. Viscoelastic phase angles of undegraded nanocomposites exhibit no significant variation with ceramic content. In a similar manner, PLGA exhibits substantially lower values of indentation hardness compared with the undegraded nanocomposites (see table 1).

Elastic moduli and viscoelastic phase angle information for PLGA specimens degraded for 0, 7 and 11 days is given in figures 3c and 3d. A notable feature of moduli and phase angles is the invariance of the variables with degradation time; no evidence of hydration front effects can be observed for data acquired at 7 and 11 days. After this time point samples were too compliant for sectioning and no further data could be acquired.

Figure 4 shows the evolution of elastic moduli and viscoelastic phase angles for 10 wt%, 20 wt%, 30 wt% and 40 wt% nanocomposites with degradation time. Qualitatively all nanocomposites follow the same mechanical property evolution which is now discussed quantitatively for 30 wt% nanocomposites.

The transect elastic modulus variation at 7 days exhibits a core-peripheral structure with regions categorizable as core and periphery possessing mean elastic moduli of 6.58 ± 0.12 GPa and ~ 1 GPa respectively. Peripheral viscoelastic phase angles are also elevated relative to the core.

After 14 days the core region decreases in spatial extent as expected due to water imbibition. Peripheral elastic moduli remain approximately unchanged compared with those measured at 7 days. The hardness at the periphery also registers a minimum of approximately 100 MPa. Phase angles for the core and periphery begin to diverge and attain values of 6.6° and 25° respectively.

At $t_d = 28$ days, identification of a core region in terms of hardness or elastic modulus is not possible, the peak modulus recorded is 4.36 GPa compared with the initial undegraded elastic modulus of 6.58 GPa for the material. Core-periphery phase angle contrast is still possible with a core region mean phase angle of 7.7±0.2° and observed loss angles for the periphery in excess of 20° and 30° for some indents.

Data were acquired for 30 wt% composite degraded for 49 days although at such an advanced stage of decomposition only several test indents could be performed on the specimens. Moreover, the definition of a transect distance could not be made using reference markers on the sample boundary due to significant specimen warping. The average measured elastic modulus, hardness and phase angle were 0.56 ± 0.54 GPa, 11 ± 12 MPa and $43° \pm 34°$ respectively; the highest recorded elastic modulus for all tests was 1.1 GPa.

Increased viscoelastic phase angles and simultaneous decrease in material modulus with degradation time is indicative of material plasticization and evolution of material properties towards those of elastomers.

5 Analysis

A stiffening effect and reduction in viscosity is observed with ceramic incorporation into a PLGA(50:50) matrix which agrees quantitatively with the mechanical behaviour of similar undegraded PLGA and nanocomposites assessed as functions of temperature using DMA by Wilberforce *et al.* [21].

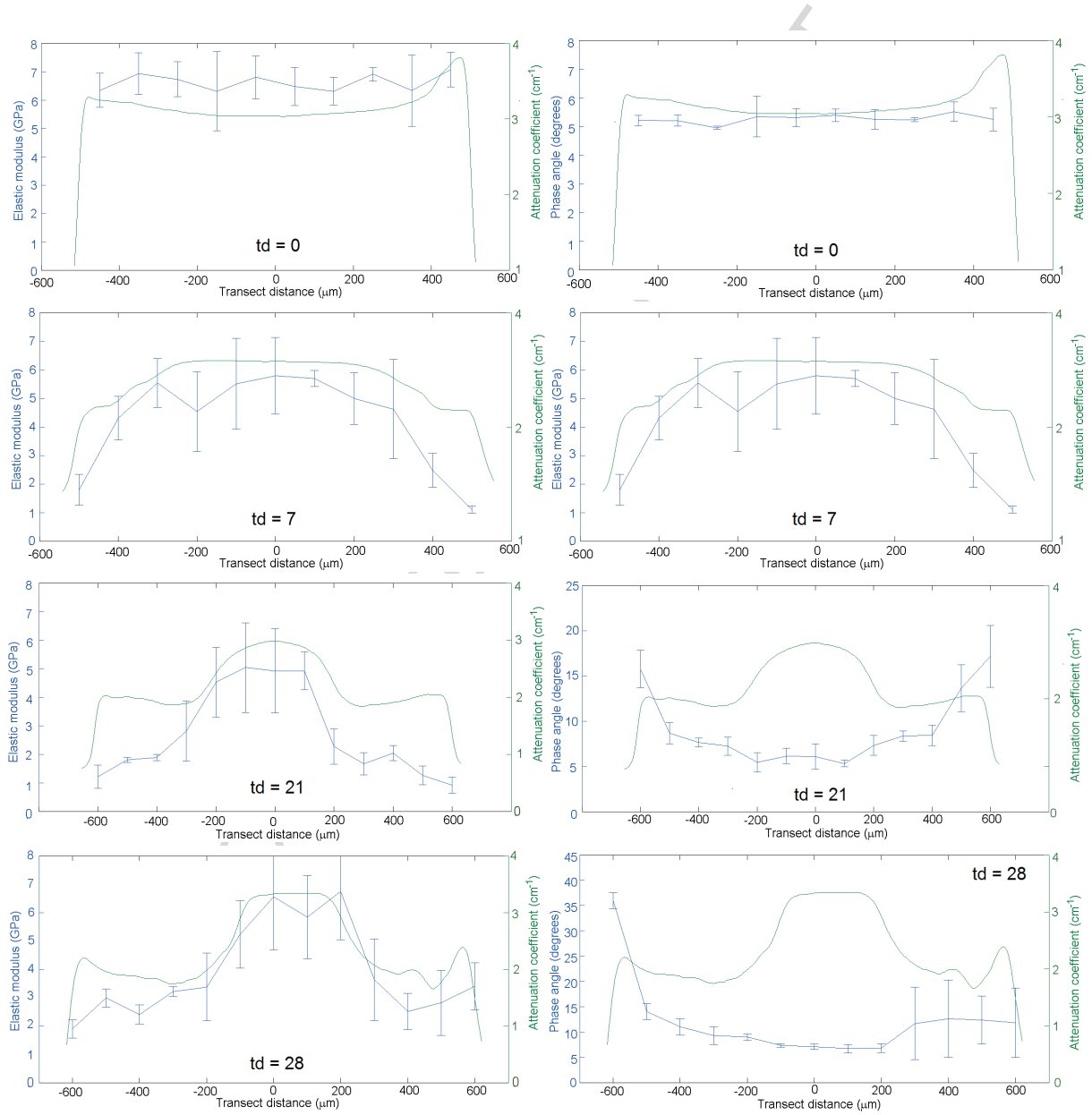

Figure 6: Comparison of elastic moduli (left) and viscoelastic phase angles (right) with XμT attenuation coefficients (measured using V_{accel}= 60 kV) for 30 wt% nanocomposites at varying degradation times. Distances are presented relative to the sample meridian.

Figure 5 shows that core region elastic moduli of nanocomposites exhibit uniform rates of elastic modulus change with degradation time; the variation between specimens arise from the different starting values of elastic modulus for undegraded materials.

Bi-phasic PLGA-TCP elastic modulus Voigt-Reuss and Hashin-Shtrikman [30] limits were calculated using literature Poisson's ratio and elastic modulus for αTCP [31] ($E = 102.4\,\text{GPa}$, $\nu = 0.275$) and the nanoindentation measured elastic modulus of 3.72 GPa for PLGA assuming $\nu = 0.4$. Limits are presented in table 1 which also includes the Voigt-Reuss limit on phase angle calculated by application of the viscoelastic correspondence principle.

Undegraded composite elastic moduli conform closely to the lower Hashin-Shtrikman limits which represent modulus limits of materials of arbitrary geometry indicating that an evenly dispersed nanoparticle system is the poorest possible bioceramic configuration state for elastic modulus enhancement. The tendency of the nanocomposite properties to the lower Hashin-Shtrikman limit contrasts with the distribution of osseous tissue properties within the bounds as measured by Oyen *et al.* [32] which is a consequence of the differing structural forms for the specimens tested.

Measured elastic moduli, for all specimens, manifest significantly greater susceptibility to changes effected by degradation and hydration compared with the phase angle. Elastic moduli and phase angles changes for 30 wt% nanocomposites with degradation time are compared with X-ray microtomographic attenuation coefficient transects in figure 6 which demonstrates that the correlation between the hydration front and elastic modulus is greater than that with the phase angle.

6 Conclusion

This paper describes the evolution of the interior mechanical properties of PLGA(50:50) and nanocomposites formed from αTCP and PLGA(50:50) with varying ceramic loadings. This is the first known instance of systematic mechanical property evaluation for a material of this type.

Peripheral regions experience a significant increase in viscosity as evidenced by the increased viscoelastic phase angle relative to the core with peripheral region properties tending towards those of elastomers generating a core-periphery morphology which correlates well with material attenuation coefficient variations measured using X-ray microtomography.

A time-delay exists between elastic modulus reduction caused by hydration and plasticisation and associated increases in material viscosity as evidenced by higher viscoelastic phase angles. No difference in viscosity was recorded with ceramic incorporation however, all nanocomposites exhibited much lower viscosity compared with pure PLGA specimens.

More detailed characterization is required such as the effect of oscillation frequency on material properties across the range encountered physiologically. More significant is the need to evaluate material properties in a wet environment and at physiological temperatures specifically addressing *in vivo* conditions.

Acknowledgements

The authors would like to thank Miss Camille Flament for assistance in preparing specimens for nanoindentation. This work was supported by the UK EPSRC under grants EP/P502365/1 and EP/P504120/1.

References

[1] M. Vert, Polymeric biomaterials: Strategies of the past versus strategies of the future, Progress in Polymer Science, 32 (2007) 755

[2] Y.Chen, S. Zhou, Q. Li, Mathematical modelling of degradation for bulk-erosive polymers applications in tissue engineering scaffolds and drug delivery systems, Acta Biomaterialia 7 (2011) 1140

[3] C.E Barrett, R.E. Cameron, S.E. Best, Bioceramic and Biopolymer Nanocomposite Materials for Use in Orthopaedic Applications CRC Press, Taylor and Francis (2012)

[4] Z. Yang, S.M. Best, R.E. Cameron, The influence of a -tricalcium phosphate nanoparticles and microparticles on the degradation of poly(D, L-lactide-co-glycolide), Advanced Materials 21 (2009) 3900

[5] L.M. Ehrenfried, D. Farrar, D. Morsley, R.E. Cameron, Mechanical behaviour of interpenetrating co-continuous beta- TCP-PDLLA composites, Bioceramics 20 (2008) 361

[6] F. Meyer, J. Wardale, S. Best, R. Cameron, N. Rushton, R. Brooks, Effects of lactic acid and glycolic acid on human osteoblasts: A way to understand PLGA involvement in PLGA/calcium phosphate composite failure, Journal of Orthopaedic Research, 30 (2012) 864

[7] A.C. Fischer-Cripps, Nanoindentation, Mechanical Engineering Series, 2nd Ed.,Springer (2004)

[8] Y.T. Cheng, T.Page, G.M. Pharr, M. Swain, K.J. Wahl (Eds.), Fundamentals and applications of instrumented indentation in multidisciplinary research, Journal of Materials Research 19 (2004) 1

[9] I.N. Sneddon, The relation between load and penetration in the axisymmetric boussinesq problem for a punch of arbitrary profile, International Journal of Engineering Science, 3 (1965) 47

[10] N. Fujisawa, M.V. Swain, On the indentation contact area of a creeping solid during constant-strain-rate loading by a sharp indenter, Journal of Materials Research 22 4 (2007) 893

[11] W.C. Oliver, G.M. Pharr, An improved technique for determining hardness and elastic modulus using load and displacement sensing indentation experiments, J. Mater. Res. 7 (1992) 1564

[12] W.C. Oliver, G.M. Pharr, Measurement of hardness and elastic modulus by instrumented indentation: Advances in understanding and refinements to methodology, Journal of Materials Research 19 (2004) 3

[13] N.W. Tschoegl, W.G. Knauss, I. Emri, Poisson's ratio in linear viscoelasticity-A critical review, Mechanics of Time dependent materials 6 (2002)

[14] G. Feng, A.H.W. Ngan: Effects of creep and thermal drift on modulus measurement using depth-sensing indentation, Journal of Materials Research 17 (2002) 660

[15] B. Tang and A.H.W. Ngan: Accurate measurement of tip-sample contact size during nanoindentation of viscoelastic materials, Journal of Materials Research 18, 1141 (2003)

[16] A.H.W. Ngan, B. Tang, Viscoelastic effects during unloading in depth-sensing indentation, Journal of Materials Research 17 (2002) 2604

[17] Y.T. Cheng, W. Ni, C. M. Cheng: Determining the instantaneous modulus of viscoelastic solids using instrumented indentation measurements. Journal of Materials Research 20 (2005) 3061

[18] A.H.W. Ngan, H.T.Wang, B. Tang, K.Y. Sze: Correcting power-law viscoelastic effects in elastic modulus measurement using depth-sensing indentation, International Journal of Solids and Structures 42 (2005) 1831

[19] M.R. Vanlandingham, N.K. Chang, P. L. Drzal, C.C. White, S.H. Chang, Viscoelastic characterization of polymers using instrumented indentation. I. quasi-static testing, Journal of Polymer Science: Part B: Polymer Physics, 43 (2005) 1794

[20] B.D. Culity, S.R. Stock, Elements of X-Ray diffraction, 3rd Ed. Pearson Educational International (2001)

[21] S.I.J. Wilberforce, S.M. Best, R.E. Cameron, J. Mater. Sci.: Materials in Medicine 21 (2010) 3085

[22] J.C. Hay, G.M. Pharr, ASM Handbook for Mechanical Testing and Evaluation 8 (2000) 232

[23] D. Tabor, The hardness of metals, Clarendon Press, Oxford (2005)

[24] G.M. Pharr, J.H. Strader, W.C. Oliver, Critical issues in making small-depth mechanical property measurements by nanoindentation with continuous stiffness measurement, Journal of Materials Research 24 (2009) 653

[25] M.R. Vanlandringham, Review of instrumented indentation, Journal of Research of NIST 108 (2003) 249

[26] K. Durst, B. Backes, M. Goken, Indentation size effect in metallic materials: correcting for the size of the plastic zone. Scripta Materialia 52 (2005) 1093

[27] W.D. Nix, H. Gao, Indentation size effects in crystalline materials: a law for strain gradient plasticity, Journal of the Mechanics and Physics of Solids 46 (1998) 411

[28] nano-indentation, Journal of the Mechanics and Physics of Solids 54 (2006) 1668

[29] C.S. Han, Influence of the molecular structure on indentation size effect in polymers, Materials Science and Engineering A 527 (2010) 619

[30] Z. Hashin, S.S. Shtrikman, A variational approach to the theory of elastic behaviour in multiphase materials, Journal of the Mechanics and Physics of Solids 11 (1963) 127

[31] L. Liang, P. Rulis, W.Y. Ching, Mechanical properties, electronic structure and bonding of a- and b-tricalcium phosphates with surface characterization, Acta Biomaterialia 6 (2010) 3763

[32] M.L. Oyen, V.L. Ferguson, A.K. Bembey, A.J. Bushby, A. Boyde, Composite bounds on the elastic modulus of bone, Journal of Biomechanics, 41 (2008) 2585